Chapter 4

Diffusion under reaction conditions

Abstract On the basis of the experiments of Chapter 3, we propose to study the diffusion of adsorbed species under reaction conditions. Angle-resolved experiments are performed in the O-rich and CO-rich regimes for $400 \leqslant T \leqslant 490\,\mathrm{K}$. HoMF is used to obtain numerical values for the diffusion activation energy. A reaction–diffusion model is then established, with a better treatment of diffusion. And the influence of various parameters, namely the diffusion rate, the surface temperature, the effect of the support and the local angle distribution of the product is investigated.

4.1 Experimental

4.1.1 Geometry of the beams

The key point in these experiments is the tilted incidence angle of the O_2 beam. With such a setup, one side of the particles is exposed to a direct O_2 flux and the other side is shadowed and does not receive any direct flux. It thus depends on the diffusion rate of O_{ad} whether Θ_O is equilibrated at steady state or the differences remain. Conversely, the geometry of the CO beam is not important, CO_{ad} always diffuses fast compared to O_{ad} [51]. Therefore, we chose to expose the particles from the sample surface normal such that the CO exposure is symmetrical. This insures that effects of an inhomogeneity of Θ_{CO} can be neglected in the discussion. As already mentioned in Section 1.3, CO_2 does not adsorb at the Pd surface and desorbs immediately after its formation. As the maximum desorption rate is always directed along the local surface normal, AR CO_2 distributions are expected to reflect the distribution of local reaction rates over differently oriented microfacets. And since we expect Θ_{CO} to be equilibrated over the surface at steady state, the CO_2 distributions directly reflect the distribution of Θ_O at the surface.

O_2 is provided by the supersonic beam at $\phi = 35°$ or $\phi = 55°$, where ϕ is the colatitude measured from the sample surface normal. We take the convention of giving angles measured on the O_2 beam side a positive value and a negative one for measurements on the other (shaded) side. CO is provided by a single or a double effusive beam to ensure the symmetric CO exposure, see Figure 4.1. Also note that ^{13}CO is used for the experiments in order to increase the signal-to-noise ratio.

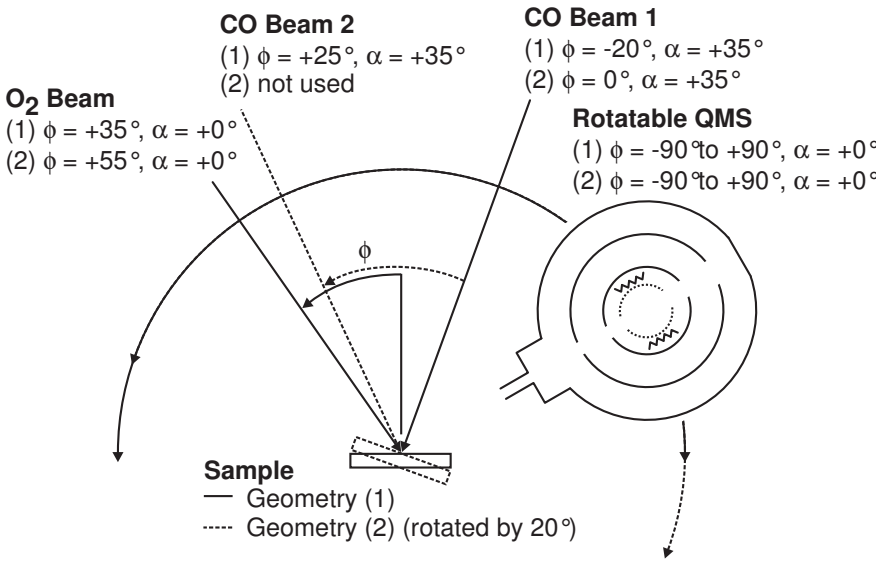

Figure 4.1. Two different geometries are used. The O_2 beam is tilted from the sample surface normal. A double (geometry 2) or single (geometry 1) CO beam is used. ϕ is the colatitude, α is the elevation from the xz-plane.

4.1.2 Elaboration of the angle resolved experiments

The method used to extract the angle distribution of CO_2 from the measurements has already been briefly described in the literature [53]. The CO_2 signal is measured on the front side of the sample from $\phi = -90°$ to $\phi = 90°$ by the AR QMS at steady state (Figure 4.2a). The diffuse background of CO_2 is determined on the backside of the sample at $\phi = -95°$ and $\phi = 95°$ and linearly subtracted from the signal. For comparison, the data are then normalized with respect to a few points around $\phi = 0°$ (Figure 4.2b and c).

The acceptance area of the AR QMS changes as a function of the detection angle [93]. We determine the detector function by using the well-defined angle distribution of Ar scattered from a flat sample covered by a thick ice (H_2O) layer at $T = 120\,\mathrm{K}$. As Ar trapping is complete under these conditions [94], detailed balance requires that the angle distribution of desorbing Ar is cosine (Figure 4.2c). Consequently, the CO_2 signal is normalized to the ratio of Ar signal to a cosine distribution. The angle distribution of desorbing CO_2 flux thus obtained is plotted in Figure 4.2d.

4.2 Size, x_{CO} and T dependence

4.2.1 Experiments

In a first step, we investigate the angle distribution of CO_2 on Sample B and Sample C. It should be noted that in spite of the lower aspect ratio for Sample B as compared to Sample C, the majority of surface atoms is still located on the side facets. Therefore, different reaction rates on the side facets should yield a significant asymmetry of the CO_2 angle distribution for both samples. Also note that Sample A is not used, since we do not expect more informations than with Sample B.

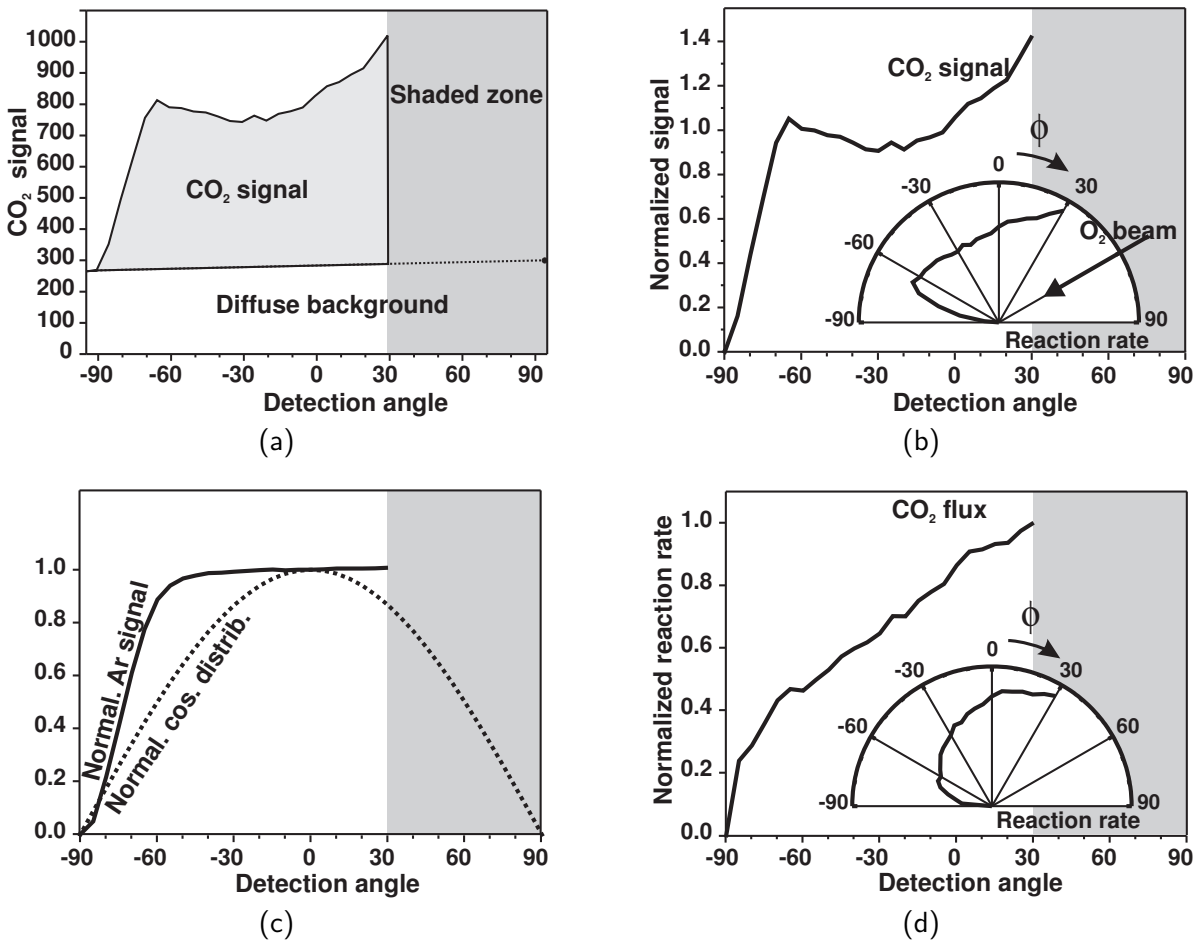

Figure 4.2. Experimental data analysis: (a) Signal measured by the AR QMS from -95° to 95°; (b) Normalized signal after background subtraction (inset on a polar plot); (c) Ar signal backscattered from an ice covered sample at 100 K and pure cosine distribution; (d) angle distribution of the CO_2 desorption rate after correction for the experimentally derived detector function (inset on a polar plot). (In the gray zone, the O_2 beam is shaded by the AR QMS.)

Size dependence

The O-rich and CO-rich reaction regimes are investigated experimentally. Representative values of $x_{CO} = 0.44$ and $x_{CO} = 0.62$, respectively, are chosen for Sample B, and $x_{CO} = 0.34$ and $x_{CO} = 0.67$ for Sample C. Figure 4.3 shows that the distributions for Sample B are symmetric under all conditions. However, the distributions for Sample C are symmetric in the O-rich regime but asymmetric in the CO-rich regime with a considerably enhanced CO_2 production on the O_2 beam side. As discussed above, the CO_2 distributions account for the local distribution of O_{ad} (or Θ_O). These results thus demonstrate that there is complete equilibration of Θ_O in the case of Sample B under all reaction conditions. Similarly, on Sample C under O-rich conditions, O_{ad} diffuses sufficiently fast over the particle to result in a complete equilibration. Whereas the equilibration does not occur under CO-rich conditions. Since we do not observe significant differences as a function of

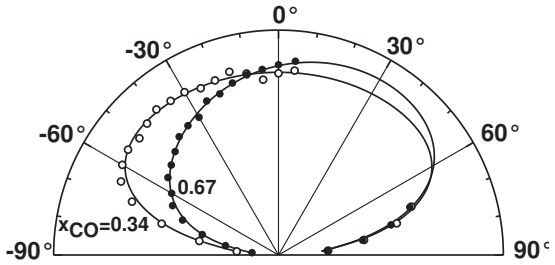

(a) Sample C, geometry 1; $T = 465$ K

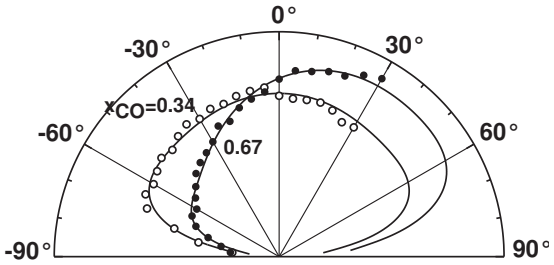

(b) Sample C, geometry 2; $T = 465$ K

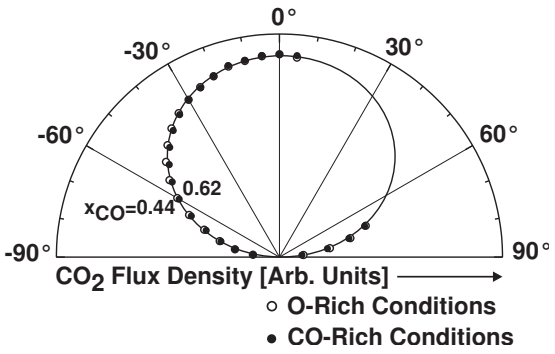

(c) Sample B, geometry 1; $T = 465$ K

Figure 4.3. Comparison of the AR distribution of CO_2 desorbing under steady state from Sample B and Sample C under O-rich (open symbols) and CO-rich (solid symbols) conditions.

x_{CO} with Sample B, the next experiments are only performed on Sample C.

x_{CO} and T dependence

The dependence of the CO_2 angle distribution on x_{CO} for Sample C is shown in Figure 4.4a. It switches within a narrow x_{CO} range from a symmetric to an asymmetric shape. The switching occurs with the transition from O-rich to CO-rich. In contrast to the pronounced influence of x_{CO}, the angle distributions exhibit detectable temperature dependence neither under O-rich (Figure 4.4b) nor CO-rich conditions (Figure 4.4c).

4.2.2 Simulations with the homogeneous mean field model

The relevant quantity that determines the equilibration of the reactant coverages on a particle is the O_{ad} diffusion length L_O during the surface residence time τ_O. The latter is determined by Θ_O at steady state and by the reaction rate $\mathcal{R}$ expressed in turnover frequency (TOF, product molecules formed per active surface atom and time),

$$\tau_O \equiv \frac{\Theta_O}{\mathcal{R}}. \tag{4.1}$$

τ_O and L_O sensitively depend on the reaction conditions. Figure 4.5a shows τ_O calculated with HoMF. As suggested by the experiments, a strong dependence of τ_O on x_{CO} is found. The transition between O-rich and CO-rich shows a sudden decrease. The latter is due to the rapidly declining Θ_O upon crossing the kinetic phase transition between the two regimes. Contrary to the strong influence of x_{CO}, the dependence of τ_O on T is moderate.

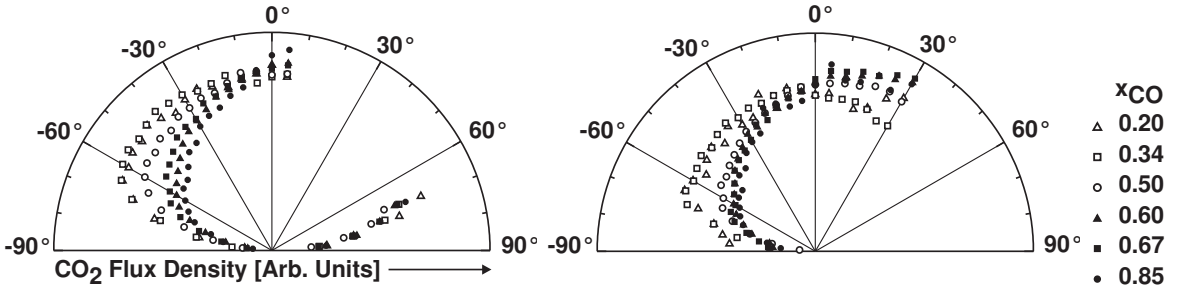

(a) x_{CO} dependence

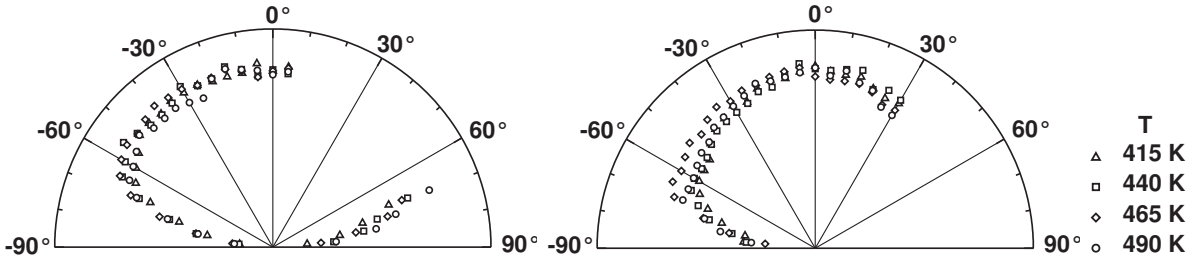

(b) T dependence; O-rich, $x_{CO} = 0.34$

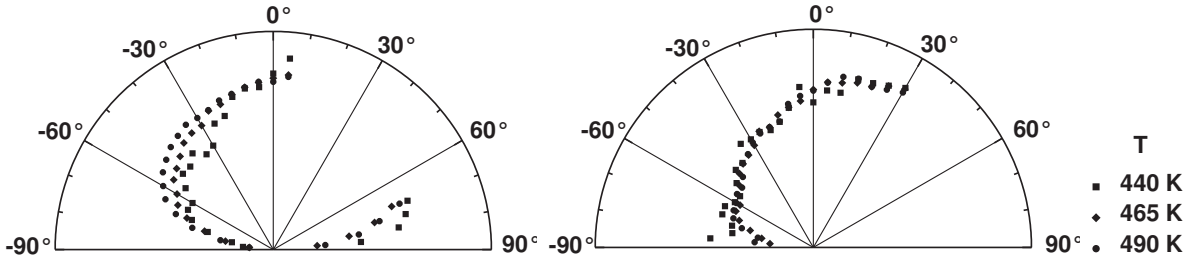

(c) T dependence; CO-rich, $x_{CO} = 0.67$

Figure 4.4. AR distributions of CO_2 desorbing at steady state from Sample C, as a function of (a) x_{CO}, (b) T under O-rich conditions and (c) T under CO-rich conditions; for both geometries described in Figure 4.1.

x_{CO} dependence

The x_{CO} dependence can be understood qualitatively. On both sides of the transition point between the O-rich and the CO-rich regime, the reaction rates are comparable but Θ_O decreases by approximately two orders of magnitude between $x_{CO} = 0.3$ and $x_{CO} = 0.7$. Eq. 4.1 implies a similar change for τ_O. As a result, L_O decreases dramatically. Complete equilibration of Θ_O does not occur and a switching from a symmetric to an asymmetric angle distribution is observed for the reaction rate as the reaction conditions go from O-rich to CO-rich.

The complete equilibration of Θ_O on Sample B under all conditions implies that L_O is larger than the particle size (5.5 nm on average). On Sample C, L_O is larger than the particle size (500 nm) under O-rich conditions, but lower under CO-rich conditions. The equilibration of O_{ad} under O-rich conditions is due to the large Θ_O. Whereas under CO-rich conditions, the depletion of O_{ad} from a small Θ_O is relatively more important.

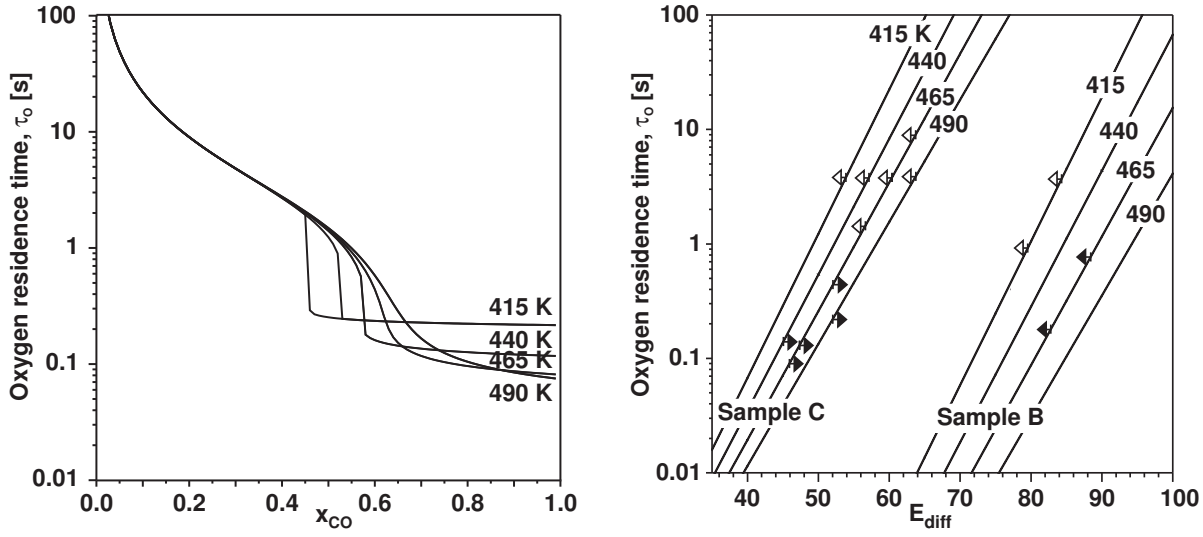

(a) HoMF (b) HoMF

Figure 4.5. (a) Oxygen residence time calculated with HoMF for Sample C. (b) Oxygen residence times required to provide a diffusion length in the order of the different particle diameters assuming an Arrhenius temperature dependence of the diffusion coefficient for different activation barriers and a pre-exponential factor of 10^{-3} cm^2 s^{-1}. The arrows indicate upper and lower limits for the diffusion barrier under CO-rich (solid symbols) and O-rich (open symbols) as derived from the AR data.

T dependence

On the O-rich side, the absence of T dependence can also be understood qualitatively. The two parameters dependent on T and having an influence on Θ_O (and therefore on the angle distributions) are $\mathcal{R}$ and τ_O. We found that $\mathcal{R}$ does not exhibit T dependences. And L_O is larger than the particle size so that an increase due to a variation of T does not have a significant influence on the Θ_O distributions. Therefore, $\mathcal{R}$ and L_O are not dependent on T under O-rich conditions. Hence, no T dependences of the distributions can be expected. These assumptions, however, do not hold in the CO-rich regime, where the moderate influence of T is likely due to two competing effects: The increased $\mathcal{R}$ with increasing T is partially compensated by an increasing Θ_O. The latter is the consequence of a decreasing Θ_{CO} at higher T due to faster desorption and reaction, resulting in a reduced inhibition of O_2 adsorption.

Oxygen diffusion barrier

Based on the results from the AR measurements and the microkinetic simulations, information on the oxygen diffusion barrier E_{diff} can be obtained. Figure 4.5b shows upper and lower limits to the activation barriers for the different reaction conditions and particle sizes. These results are based on estimates of τ_O (Figure 4.5a) required for diffusion across a particle calculated from the Einstein relation. Under CO-rich reaction conditions, a lower limit of 50 ± 5 kJ mol^{-1} (Sample C) and an upper limit of 85 ± 5 kJ mol^{-1} (Sample B) are obtained for E_{diff}. Whereas under O-rich conditions, we find an upper limit of

$60 \pm 5\,\mathrm{kJ\,mol^{-1}}$ (Sample C).

So far, no quantitative experimental data for oxygen diffusion on Pd single crystal are available, which could be compared to the present results. However, the value is in good agreement with recent theoretical investigations predicting a diffusion barrier $E_{\mathrm{diff}} = 54\,\mathrm{kJ\,mol^{-1}}$ on Pd(111) [95]. Nonetheless, such comparisons should be treated with care as the present measurements correspond to a surface under reaction conditions, i.e., at high coverages, whereas the calculations are typically performed in the low coverage limit. Adsorbate interactions at high coverages are expected to significantly influence the diffusion activation energies. In addition, there might be significant contributions from particle-specific sites such as steps, edges, and defects to the effective diffusion rates on a metal nanoparticle.

4.3 Establishment of the reaction–diffusion model

There are important limitations concerning HoMF for diffusion studies. The angle distribution from a given site sensitively depends on the presence of coadsorbed species [46, 96]. This complicates a quantitative analysis with simple MF models, where diffusion is not treated realistically. Here, HoMF assumes infinitely fast diffusion of the adsorbates: this assumption is acceptable concerning CO_{ad} but not O_{ad}. Moreover, the model assumes infinite flat surfaces, however Sample C consists of an array of 500 nm high towers of Pd. HoMF then becomes rapidly inadequate and we propose to implement the morphology of Sample C as well as diffusion. The new model, however, should retain the information gained from HoMF. It thus consists in a reaction–diffusion (RD) type of model. The reaction part is based on HoMF and diffusion is treated by means of Fick laws. Morphology is implemented together with diffusion.

4.3.1 Reaction–diffusion scheme

Diffusion

Adsorbates remaining in a chemisorbed state can move at the surface. The simplest diffusion mechanism is hopping of the adsorbate to the nearest equivalent site but more complicated mechanisms have also been reported, see, e.g., Ref. [97].

CO_{ad} diffuses fast on close-packed surfaces [51, 98]. Complete equilibration of Θ_{CO} at the surface can then be assumed at the timescale of the simulations. This is mathematically represented by averaging Θ_{CO} over the surface ($\overline{\Theta_{CO}}$). Diffusion of O_{ad} is treated by the first Fick law as

$$\frac{\partial \Theta_O}{\partial t} = \mathcal{D}\nabla^2\Theta_O. \tag{4.2}$$

Where $\mathcal{D}$, the diffusion coefficient, is assumed to follow an Arrhenius T dependence

$$\mathcal{D} = \nu_{\mathrm{diff}} \exp\left(\frac{-E_{\mathrm{diff}}}{RT}\right).$$

Little experimental data are available on the diffusion coefficient for O_{ad} on Pd(111). A "normal" value of $\nu_{diff} = 10^{-3}\,cm^{-2}\,s^{-1}$ for the preexponential factor is thus assumed [51]. Possible values for E_{diff} are investigated in Section 4.4.2, otherwise, a value $E_{diff} = 55\,kJ\,mol^{-1}$ is assumed as found in the previous section. For simplicity, we neglect the coverage dependence of $\mathcal{D}$.

Reaction–diffusion

The diffusion is introduced into HoMF according to a RD scheme. That is combining Eq. 3.4 and Eq. 4.2,

$$\frac{d\Theta_{CO}}{dt} = w^{ad}_{CO}(\Theta_O, \Theta_{CO}) - w^{des}_{CO}(\Theta_{CO}) - w_{LH}(\Theta_O, \Theta_{CO}), \tag{4.3a}$$

$$\frac{d\Theta_O}{dt} = 2w^{ad}_{O_2}(\Theta_O, \Theta_{CO}) - w_{LH}(\Theta_O, \Theta_{CO}) + \mathcal{D}\nabla^2\Theta_O. \tag{4.3b}$$

Morphology

Sample C is represented by a half prolate spheroid with height $c = 450\,nm$ and equatorial radius $a = 250\,nm$ according to the structural parameters (Section 2.2.2). The support is described by a disc of radius $r \approx 25\,\mu m$. The system is represented in a (r, θ, ϕ) spherical system of coordinates, with r radius, $0 \leqslant \theta < 2\pi$ the azimuth and ϕ the colatitude on which the convention mentioned above is kept ($\phi \geqslant 0$ on the O_2 beam side; $\phi < 0$ on the shaded side). A schematic representation is given in Figure 4.6. The particle is discretized with 400 surface elements ($\theta \times \phi = 20 \times 20$) and the support into 20,000 surface elements ($r \times \theta = 1000 \times 20$).

Flux of incident molecules

In a first step, the reactant fluxes (F_{CO}, F_{O_2}) are calculated at each surface element of the particle and of the support. F_{CO} is incident from $\phi = 0°$ to lead to a symmetric flux distribution. F_{O_2} is incident from $(\theta = 0°, \phi = 60°)$. The latter results in a partial shading of the particle as well as of the support on the side opposite to the beam, i.e., some surface elements do not receive any direct O_2 flux. In addition to the direct flux, molecules can impinge on the support. As the interaction of both reactants with SiO_2 is weak, CO and O_2 might either be trapped for a short time in a physisorbed state and subsequently desorb (trapping–desorption channel) or might be directly backscattered into vacuum (direct inelastic scattering channel). We do not distinguish between these processes and we refer to the sum of both channels as the backscattering component from the support. Moreover, there is no explicit incorporation of molecules trapped on the support and diffusing to the particles. A fraction of this backscattered flux collides with the Pd particles and leads to additional CO and O_2 fluxes. This is particularly relevant on the parts of the catalyst particle that receive little or no direct fluxes. Both trapping–desorption and direct scattering channels are expected to be rather diffuse from

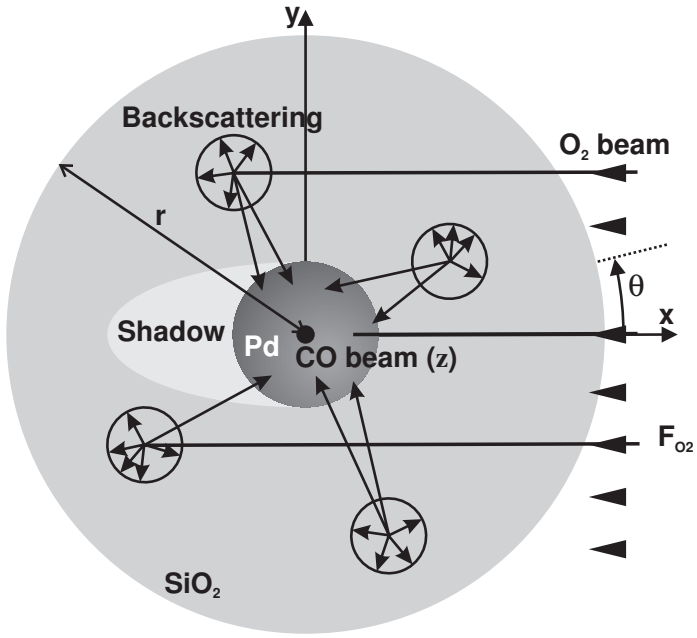

(a) RD: top view

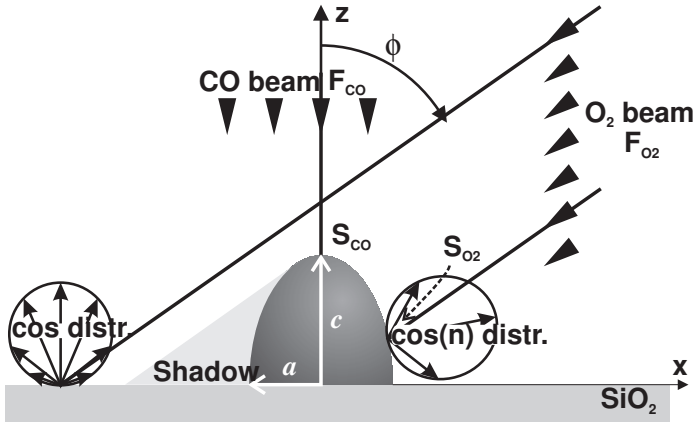

(b) RD: side view

Figure 4.6. RD; the Pd particle is represented as a half prolate spheroid (polar radius $c = 450$ nm, equatorial radius $a = 250$ nm) sitting on a support disk of $r \approx 25$ µm diameter. The CO flux is incident from $\phi = 0°$ and the O_2 flux from $\phi = 60°$, $\theta = 180°$ where the particle and the support receive no direct flux from the O_2 beam. The backscattering of the reactants and products from the support is also included.

the SiO_2 support. The backscattering contribution is therefore modeled assuming a cosine distribution for both CO and O_2. It should be noted that the backscattered fluxes onto the particle are different for O_2 and CO, due to the shadow of the particle on the support, which only exists for O_2 (see Figure 4.7). The role of support backscattering for the present type of experiments is investigated in Section 4.4.4.

After the local reactant fluxes are established, the non-spatial part of Eq. 4.3 can be integrated for any initial (Θ_{CO}, Θ_O) distribution. In a second step, the spatial part of Eq. 4.3 is integrated using the finite element method with periodic boundary conditions on θ and no fluxes across $\phi = 90°, \forall\theta$. The physical meaning of the latter is that we do not take surface diffusion from the oxide to the particle or vice-versa into account. This simplification is justified by the large particle size and by the weak interaction of the reactants with the support. Indeed, estimates of the size of adsorbate capture

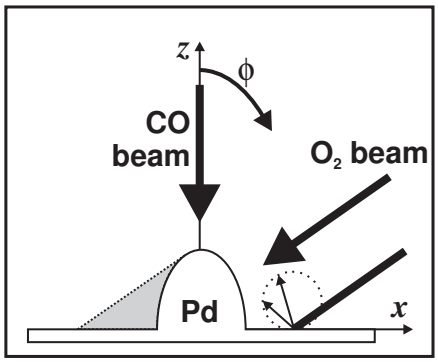

(a) Model for the incident flux

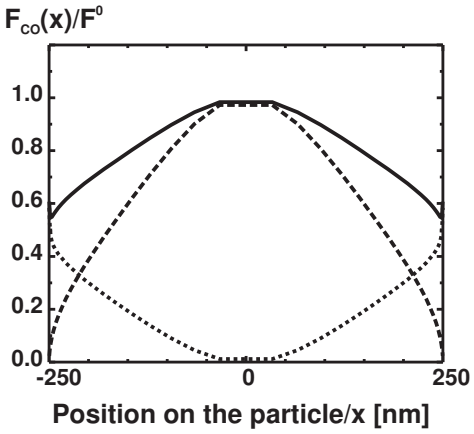

(b) F_{CO} profile along the x-axis

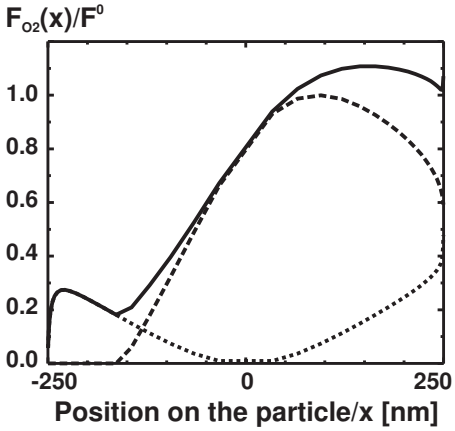

(c) $F_{\mathrm{O_2}}$ profile along the x-axis; geometry 1, with $\mathrm{O_2}$ beam from $\phi = +35°$

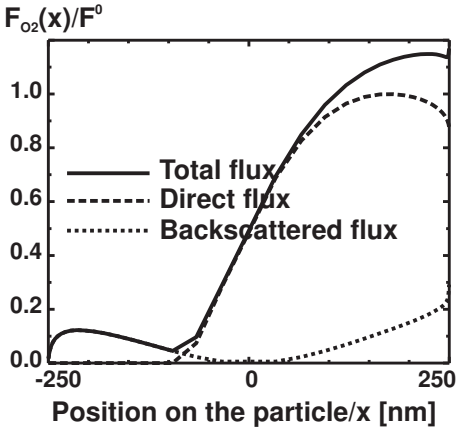

(d) $F_{\mathrm{O_2}}$ profile along the x-axis; geometry 2, with $\mathrm{O_2}$ beam from $\phi = +55°$

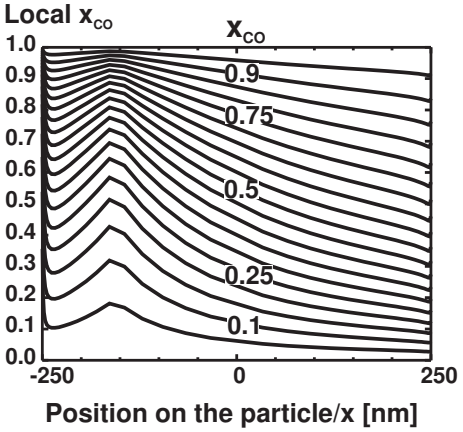

(e) x_{CO} profile along the x-axis; geometry 1

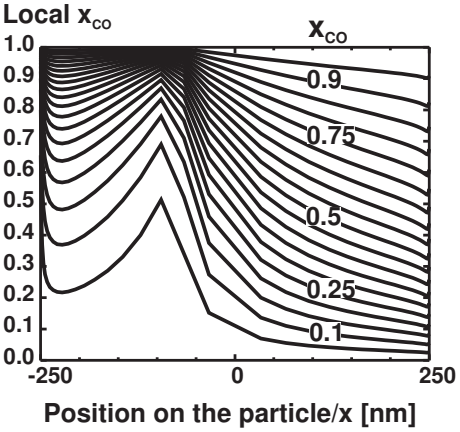

(f) x_{CO} profile along the x-axis; geometry 2

Figure 4.7. RD; flux profiles along the x-axis for the $\mathrm{O_2}$ and CO beam fluxes and the corresponding x_{CO} profiles, for both experimental geometries.

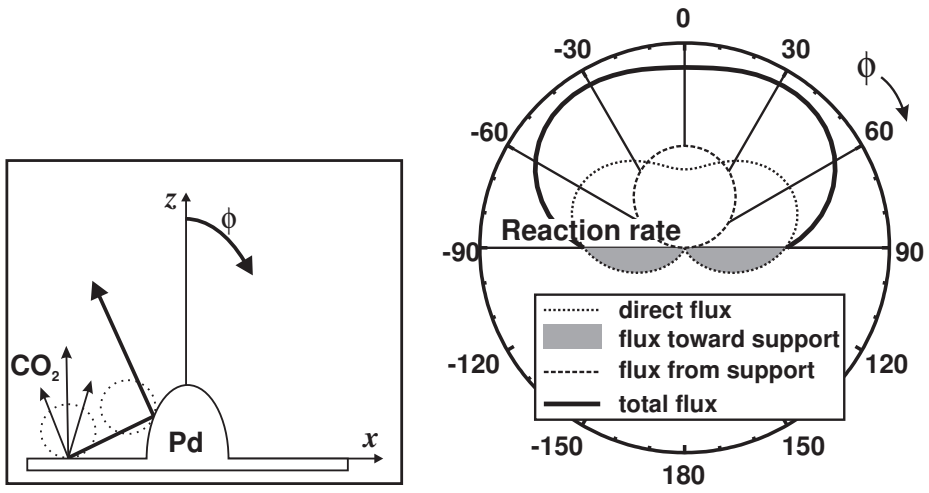

(a) Model for the reactant flux (b) Reactant flux including backscattering

Figure 4.8. RD; model for the backscattering.

zones on similar systems under reaction conditions are typically in the range of a few nanometers [31,35,99]. Thus, we expect that the adsorbate flux via surface diffusion over the particle–support interface is negligible as compared to the direct flux.

Flux of reaction products

The angle distribution of CO_2 desorbing from a Pd area element is modeled by a $\cos^n$ distribution. $n = 1$ was found experimentally for CO oxidation on Pd(111) in the limit of low coverages [46]. However, more highly directed distributions are possible at higher coverages [96]. In Section 4.4.5, we investigate the effect of the local CO_2 distribution on the type of AR experiments discussed in this work. In general, $n = 1$ is in good agreement with our experimental results and is used elsewhere.

In analogy to the reactants, CO_2 can be emitted into vacuum or collide with the support upon desorption. In the latter case trapping–desorption is also taken into account. Product backscattering depends on both CO_2 distribution and particle shape. The total CO_2 flux toward the support is calculated by integration over the lower half unit sphere. Afterward, the flux is reemitted into vacuum assuming a cosine distribution. The direct and backscattered product channels are added and constitute the full CO_2 angle distribution as shown in Figure 4.8.

4.3.2 Validation of the model

The kinetic model is validated by a simulation of the global steady state versus x_{CO} and T (by integration over the full particle surface) (Figure 4.9a, cf. Figure 3.1). It shows a good agreement with the experiments under all conditions (Section 3.1). Both T dependence and the transition point between the two regimes are well reproduced.

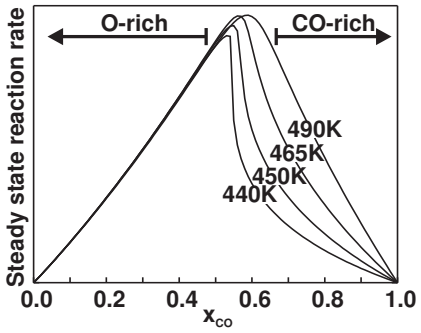

(a) RD, $E_{\text{diff}} = 55\,\text{kJ mol}^{-1}$; CO_2 reaction rate

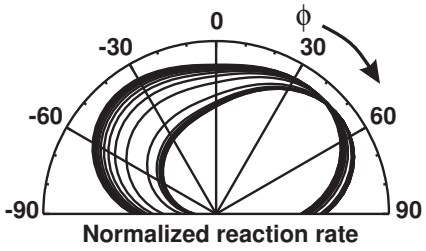

(b) RD, $E_{\text{diff}} = 55\,\text{kJ mol}^{-1}$; $T = 465\,\text{K}$; AR CO_2 distribution

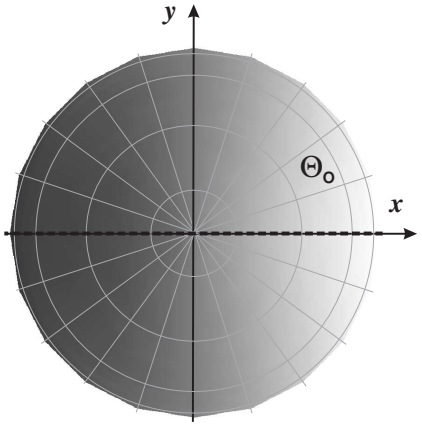

(c) RD, $E_{\text{diff}} = 55\,\text{kJ mol}^{-1}$; $T = 465\,\text{K}$; Θ_O distribution (top view) for x_{CO}=0.7 (black: low Θ_O; white: high Θ_O)

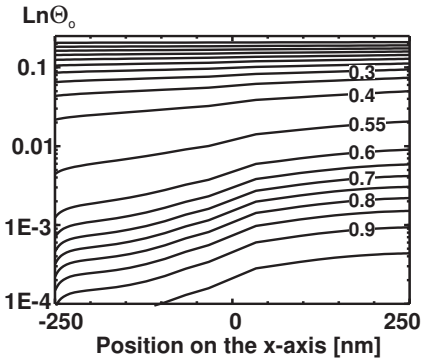

(d) RD, $E_{\text{diff}} = 55\,\text{kJ mol}^{-1}$; $T = 465\,\text{K}$; Θ_O profiles along the x-axis, by steps of 0.05

Figure 4.9. RD; (a) and (b) the AR distribution of desorbing CO_2 is symmetric in the O-rich regime ($x_{CO} < 0.5$) and asymmetric in the CO-rich regime; (d) Θ_O profiles as a function of x_{CO}.

4.4 Simulations with the reaction–diffusion model

4.4.1 Influence of x_{CO}

First, we investigate the local variations of Θ_O and $\mathcal{R}$. Θ_O at steady state on the surface of the catalyst particle at $T = 465\,\text{K}$ and $x_{CO} = 0.7$ is displayed in Figure 4.9a (white: high Θ_O, black: low Θ_O). Θ_O is significantly higher on the side facing the O_2 beam. Thus it is not equilibrated over the surface under CO-rich conditions.

As already mentioned, Θ_O distributions are assumed to directly reflect changes in local reaction rates. We thus compare the Θ_O profiles along the x-axis ($y = 0$) (Figure 4.9d) and the results from the simulations of the AR distributions for $0.05 \leqslant x_{CO} \leqslant 0.95$ at $T = 465\,\text{K}$ (Figure 4.9b).

- $x_{CO} < 0.4$, in the O-rich regime, the $\ln \Theta_O$ profiles are almost flat. They approach saturation coverage ($\Theta_O^{\max} = 0.25$) for the lowest x_{CO}. With increasing x_{CO}, conversely, Θ_O decreases and a gradient $\left(\frac{d \ln \Theta_O}{dx}\right)$ appears. As expected, flat $\ln \Theta_O$ profiles give broad symmetric CO_2 distributions. With increasing x_{CO}, nearly no

changes in the angle distributions are observed until the transition to CO-rich occurs.

- $0.4 \leqslant x_{CO} < 0.6$, in the transition between O-rich and CO-rich, the profiles change rapidly and the ratio between Θ_O on the shaded side and Θ_O on the beam side becomes very large. Here, the angle distributions become rapidly asymmetric, with a strongly enhanced CO_2 production on the O_2 beam side, where the profiles find their maximum.

- $0.6 \leqslant x_{CO}$, in the CO-rich regime, the $\ln \Theta_O$ gradients are nearly constant while the absolute $\ln \Theta_O$ decrease rapidly. As a result, the constant gradients lead only to minor changes in the angle distributions.

A comparison of the simulations to the experiments (Section 4.2.1) shows that the simulations accurately reproduce the angle distributions and their behavior as a function of x_{CO}.

4.4.2 Influence of the surface diffusion rate

In Section 4.2.2, E_{diff} is estimated with HoMF on the basis of τ_O and L_O. RD allows to give explicit values for E_{diff}. A direct comparison to the experimental angle distributions should then lead to a more accurate estimate. Simulated CO_2 angle distributions for E_{diff} ranging from $35\,kJ\,mol^{-1}$ to immobile O_{ad} under conditions comparable with the experiments (i.e., $x_{CO} = 0.34$, $x_{CO} = 0.67$ and $T = 465\,K$) are shown in Figure 4.10.

- $E_{diff} \leqslant 35\,kJ\,mol^{-1}$, the oxygen distribution is homogeneous, both under O-rich and CO-rich conditions. This indicates an equilibration of Θ_O over the particle surface independent of the reaction conditions. As a consequence, the CO_2 distributions are symmetric and independent of x_{CO}.

- $E_{diff} = 45\,kJ\,mol^{-1}$, a weak gradient is found in the Θ_O profile under CO-rich conditions leading to a slight asymmetry in the CO_2 distribution. Whereas under O-rich conditions, the distribution remains symmetric. As discussed in Section 4.2.1, this is a result of τ_O being typically 1 to 3 orders of magnitude larger under O-rich conditions, thus allowing for the equilibration of Θ_O at higher E_{diff}.

- $E_{diff} = 55\,kJ\,mol^{-1}$, a larger Θ_O gradient is established, giving rise to a strongly asymmetric CO_2 distribution under CO-rich conditions. Conversely, the distribution remains symmetric under O-rich conditions.

- $E_{diff} \geqslant 65\,kJ\,mol^{-1}$, the Θ_O profiles finally show pronounced gradients under both O-rich and CO-rich conditions, leading to asymmetric distributions. In the case of immobile O_{ad} (no diffusion), it is noteworthy that a dip appears in the Θ_O profiles on the shaded side of the particle. It is the result of a minimum in the local O_2 flux impinging on the particle. The local flux is the sum of the direct beam flux and the backscattering of reactants from the support. Due to the particle geometry, the

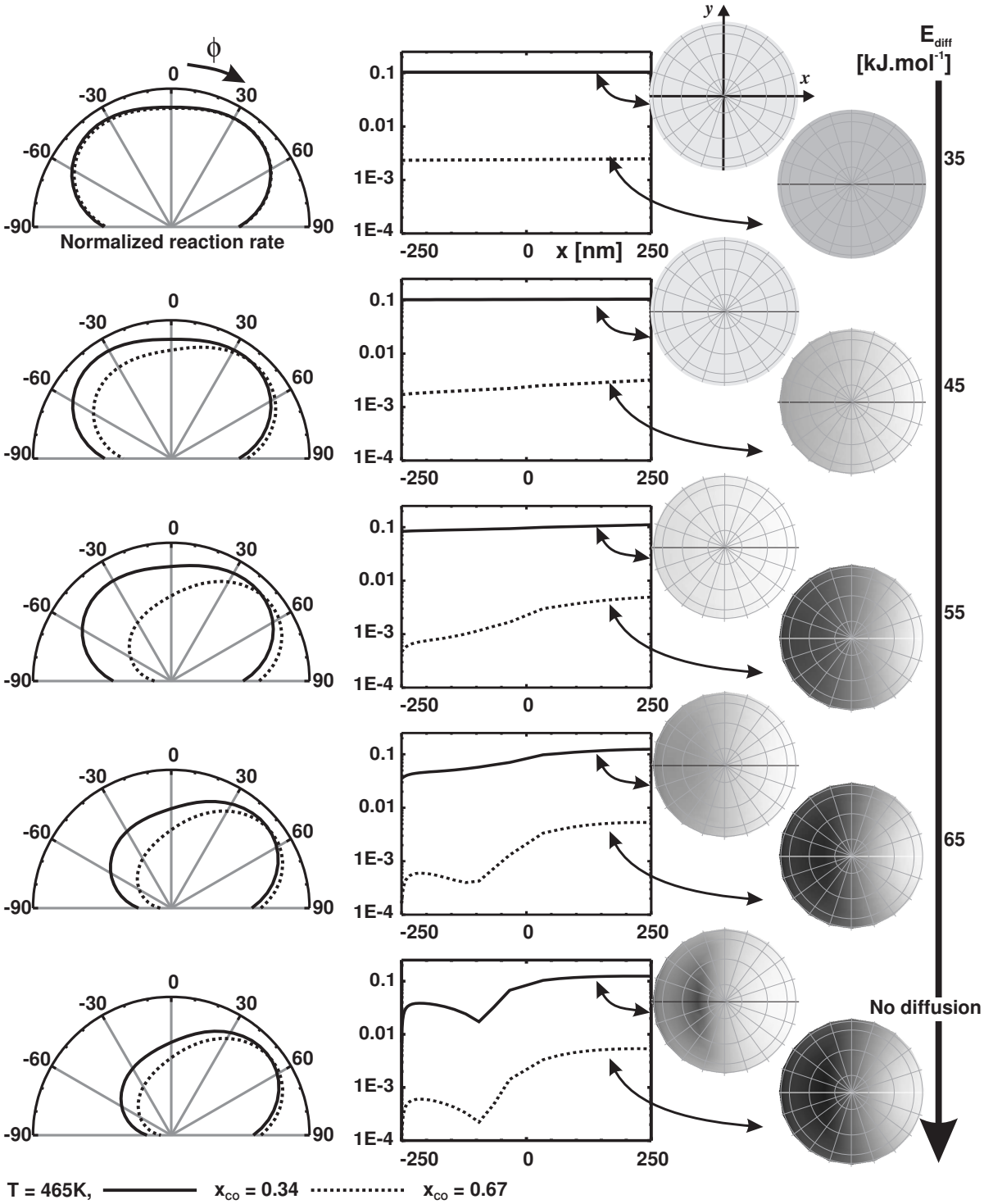

Figure 4.10. RD; $T = 465\,\mathrm{K}$. The role of oxygen diffusion investigated for $E_{\mathrm{diff}} = 35$, 45, 55, 65 kJ mol^{-1} and no diffusion; the O-rich ($x_{\mathrm{CO}} = 0.34$) and CO-rich ($x_{\mathrm{CO}} = 0.67$) regimes are compared. Left to right: angle distribution of CO_2, Θ_{O} along the x-axis of the particle and top view of Θ_{O} distribution on the particle surface (black: low Θ_{O}, white: high Θ_{O}).

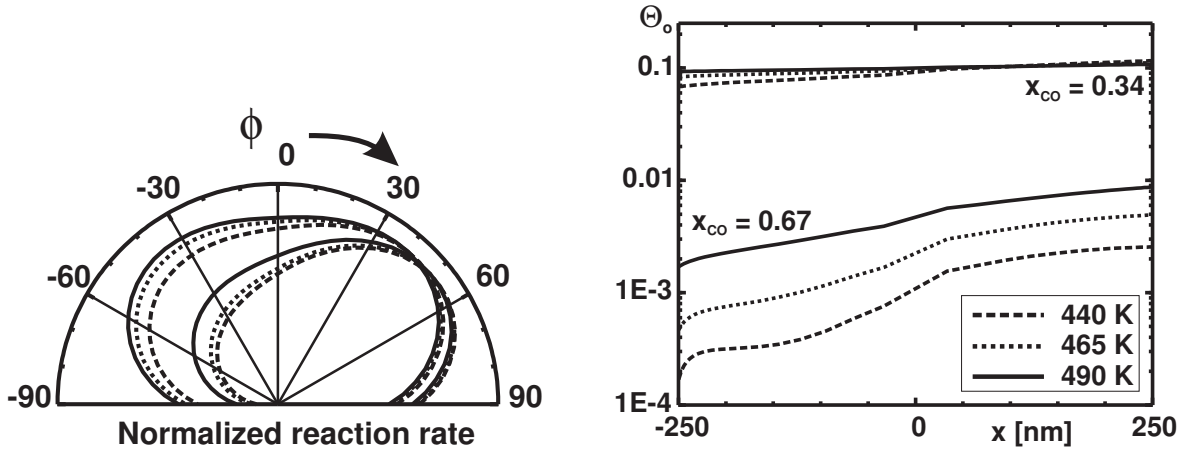

(a) RD, $E_{\text{diff}} = 55\,\text{kJ}\,\text{mol}^{-1}$; CO_2 angle distribution

(b) RD, $E_{\text{diff}} = 55\,\text{kJ}\,\text{mol}^{-1}$; Θ_O profiles

Figure 4.11. Temperature dependence of (a) the angle distributions of CO_2 and (b) Θ_O profiles.

latter contribution is enhanced in the vicinity of the particle support. This effect is discussed in detail in Section 4.4.4.

Comparison of these results to the experiments of Section 4.2.1 allows to estimate $E_{\text{diff}} = 55 \pm 10\,\text{kJ}\,\text{mol}^{-1}$ under reaction conditions. This value is in full agreement with our previous estimate calculated with HoMF in Section 4.2.2 and with the theoretical calculations mentioned in Ref. [95].

4.4.3 Influence of T

In the next step, we investigate the dependence of the angle distributions of CO_2 on the surface temperature. As shown in Figure 4.11, the model yields a weak dependence in the range $440 \leqslant T \leqslant 490\,\text{K}$ under O-rich and CO-rich conditions. Qualitatively, the distributions remain symmetric for O-rich and asymmetric for CO-rich. And in general, there is a very slight decrease in $\mathcal{R}$ on the shaded particle side with decreasing T, which tends to increase the asymmetry.

A comparison with the experiments in Figure 4.3 shows that the simulations reproduce the temperature dependence well. The simulations give a deeper insight into the kinetic origin of the temperature dependence. To summarize, Θ_O profiles and consequent CO_2 angle distributions are controlled by L_O. The latter depends on τ_O and on the diffusion coefficient $\mathcal{D}$. τ_O depends in turn on Θ_O and $\mathcal{R}$ at steady state.

O-rich conditions Θ_O is high and $\mathcal{R}$ is nearly independent of T (CO adsorption is the RDS). Therefore, τ_O is nearly independent of T. In contrast, $\mathcal{D}$ increases with T. For $E_{\text{diff}} = 55\,\text{kJ}\,\text{mol}^{-1}$, $\mathcal{D}_{490\,\text{K}}/\mathcal{D}_{440\,\text{K}} = 4.6$. However, the increase only has a moderate effect on the Θ_O profiles since L_O is already larger than the particle size at 440 K. As a result, changes in the CO_2 angle distributions are weak.

CO-rich conditions Figure 4.9a and Figure 4.11b show that both $\mathcal{R}$ and Θ_O increase with T (O_2 adsorption is the RDS and the adsorption rate of O_2 increases as Θ_{CO} decreases, i.e. with increasing T). The common increase of $\mathcal{R}$ and Θ_O compensates and leads to a weak temperature dependence of τ_O. The temperature dependence of L_O is therefore mainly due to the diffusion coefficient. The Θ_O gradient decreases slightly as L_O, which is below the particle size, increases. Consequently, the asymmetry of the angle distribution becomes less pronounced.

In the temperature interval considered, changes in Θ_O due to the temperature dependence of L_O are considerably weaker than those due to the reaction regime. The CO_2 angle distributions are more sensitive to x_{CO} than T.

4.4.4 Influence of backscattering from the support

The desired experimental information in the AR experiments is carried primarily by molecules desorbing from the Pd particles and flying directly into the detector. In practice however, there exists two additional channels:

- Incident molecules can be diffusely backscattered from the support and subsequently collide with the metal particles. This leads to a diffuse flux of reactants toward the particles.

- Reaction products desorbing from the side facets of the particles can collide with the support and be backscattered into vacuum.

It is important to determine how these contributions affect the experimental results and to what extent they might complicate the extraction of information on local reaction rates.

Backscattered flux of incident molecules

The total CO and O_2 fluxes toward the particle surface are plotted in Figure 4.7 for a section of the particle along the x-axis. The total flux contains two components, the direct beam contribution and the backscattering contribution. Whereas the direct flux is maximal at the parts of the particle directly facing the beams, backscattering is the most prominent at the edge. There are substantial differences in the backscattered fluxes of CO and O_2. The particles are exposed to CO from top. Hence, the contribution of the backscattered flux is symmetric. It approaches 50% of the maximum direct flux at the edge of the particle and vanishes on top. The O_2 beam is tilted from the sample surface normal. Hence, a large fraction of the particle as well as part of the support are shaded from a direct flux. The backscattering contribution is thus asymmetric. As a result, the total O_2 flux on the shaded side is relatively low even when support backscattering is taken into account. It is also noteworthy that support backscattering creates a zone at $x \approx 100\,\text{nm}$ where the flux has a local minimum.

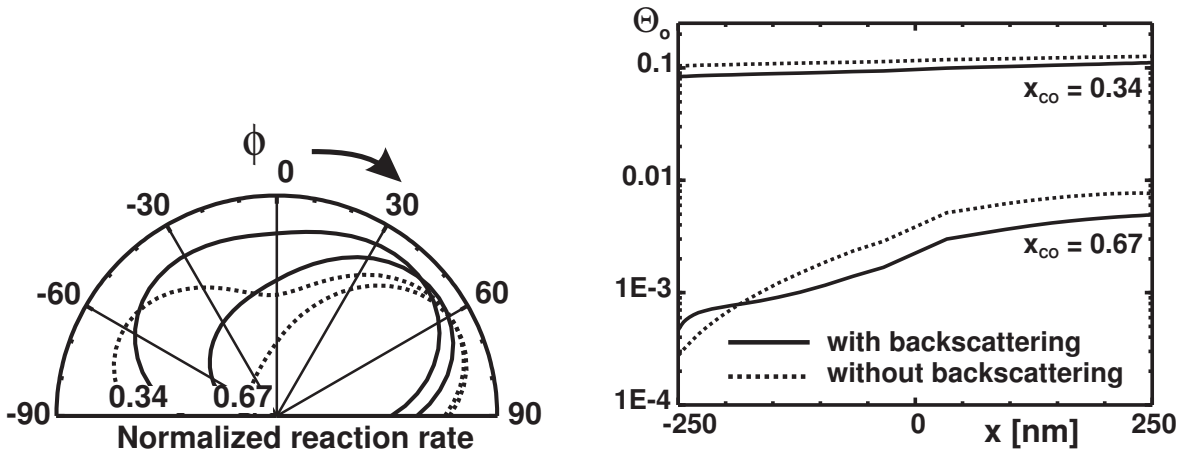

(a) RD, $E_{\mathrm{diff}} = 55\,\mathrm{kJ\,mol^{-1}}$; CO_2 angle distribution; x_{CO} indicated on the graph

(b) RD, $E_{\mathrm{diff}} = 55\,\mathrm{kJ\,mol^{-1}}$; Θ_O profiles

Figure 4.12. Backscattering dependence of (a) the angle distributions of CO_2 and (b) Θ_O profiles.

Backscattered flux of reaction products

In addition, backscattering of products is taken into account as described in Section 4.3.1. From Figure 4.8b, we find that product backscattering simply adds a symmetric component to the angle distribution of CO_2.

It is now interesting to investigate the effects of both backscattering contributions on the total angle distribution. Figure 4.12 displays Θ_O profiles and CO_2 angle distributions for a hypothetical case, in which support backscattering is completely neglected, and for a case in which the effect is taken into account ($T = 465\,\mathrm{K}, E_{\mathrm{diff}} = 55\,\mathrm{kJ\,mol^{-1}}$).

Under O-rich conditions, the differences between the models are weak on the Θ_O profiles (Figure 4.12b). Fast O_{ad} diffusion cancels the gradient in Θ_O regardless of the flux distribution. Whereas under CO-rich conditions, the gradient in Θ_O is significantly reduced by support backscattering. Here, backscattering of O_2 gives rise to a strong relative enhancement of the O_2 flux on the shaded side of the particle.

The corresponding CO_2 angle distributions are displayed in Figure 4.12a. Support backscattering results in a drastic modification of the distributions under both O-rich and CO-rich conditions. In the O-rich regime, the width of the CO_2 distributions is reduced by the backscattered flux of products. In the CO-rich regime conversely, the differences result from both reactant and product backscattering. The effect is particularly strong on the shaded side, where backscattering tremendously enhances the CO_2 production and thus effectively reduces the asymmetry of the distributions.

Comparison with the experiments Section 4.2.1 shows that the model including support backscattering reproduces the experiments more accurately. And neglecting the backscattering channel predicts artificially broad angle distributions and strongly overestimates the asymmetry.

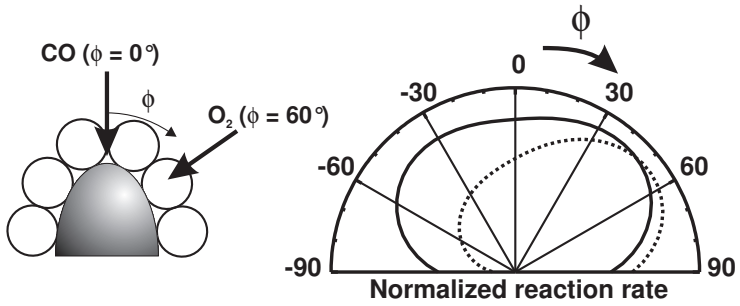

(a) RD, $E_{\mathrm{diff}} = 55\,\mathrm{kJ\,mol^{-1}}$, $T = 465\,\mathrm{K}$; $\cos^1\phi$

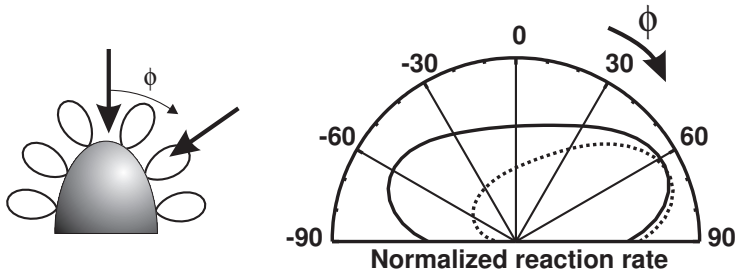

(b) RD, $E_{\mathrm{diff}} = 55\,\mathrm{kJ\,mol^{-1}}$, $T = 465\,\mathrm{K}$; $\cos^4\phi$

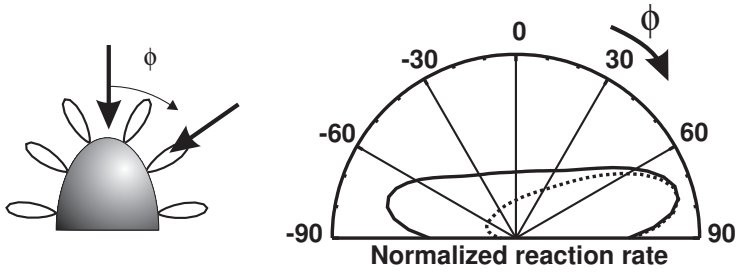

(c) RD, $E_{\mathrm{diff}} = 55\,\mathrm{kJ\,mol^{-1}}$, $T = 465\,\mathrm{K}$; $\cos^{16}\phi$

Figure 4.13. Effect of the local angle distribution of CO_2 on the total AR distribution of products desorbing from Sample C; full lines: O-rich, $x_{\mathrm{CO}} = 0.34$; dashed lines: CO-rich, $x_{\mathrm{CO}} = 0.67$.

4.4.5 Influence of the local angle distribution of CO_2

A key point in the simulation of the CO_2 angle distribution from a supported nanoparticle is the distribution from a surface element. From single crystal studies it is well known that such distributions sensitively depend on many factors such as local surface structure and coverages [100]. For Sample C, the prolonged heat treatment after preparation leads to a reshaping of the particle, preferentially exposing low-index facets. There, some experimental information is available for the angle distribution. On Pd(111) and in the limit of low coverages, the CO_2 distribution is broad and well described by a cosine distribution [46]. In the limit of high Θ_{O}, however, much stronger peaking along the surface normal is observed [96].

In the following, we investigate the role of the width of the local angle distribution on the total CO_2 distribution emitted by the supported catalyst. In the simulations, the local distribution of desorbing CO_2 is described by a function $\cos^n$. Some representative results are given in Figure 4.13, ranging from diffuse desorption ($n = 1$) to highly directed

desorption along the particle surface normal ($n = 16$). We find that the total CO_2 distribution becomes increasingly broad with increasing n. In spite of the strong dependence on the width of the local distribution, the qualitative picture remains unchanged. Under O-rich conditions, the CO_2 distributions are symmetric, whereas they become strongly asymmetric in the CO-rich regime. Although the asymmetry shows the expected decrease with decreasing n, the effect remains clearly visible down to $n = 1$.

A $\cos^n$ distribution of CO_2 from a surface element with $n = 1$ gives the best agreement with the experiments in Section 4.2.1.

4.5 Summary

We have studied the angle-resolved distribution of CO_2 desorbing from oxide-supported Pd nanoparticles at steady state during CO oxidation. We presented evidences for variations of the local reaction rate due to limited surface mobility of O_{ad} on Sample C (500 nm diameter). Whereas on Sample B (5.5 nm diameter on average,) diffusion of O_{ad} is sufficiently fast to result in a complete equilibration of Θ_O. These variations of the CO_2 angle distributions are analyzed as a function of particle size, surface temperature and reactant fluxes on the basis of HoMF. The model is utilized to extract data on surface diffusion rates on the catalyst particles under reaction conditions. These primary results are used to implement the diffusion process in HoMF by means of a reaction–diffusion scheme.

Comparisons of the simulations using RD with the experiments lead to significant new informations concerning diffusion under reaction conditions:

- The different angle distributions of CO_2 in the two reaction regimes (O-rich and CO-rich) are related to pronounced differences in the oxygen residence time. As a result, equilibration of Θ_O occurs under O-rich conditions only, and pronounced gradients in Θ_O are established under CO-rich conditions.

- Comparison of the experimental angle distributions with the simulations as function of x_{CO} gives an estimate for the activation energy for oxygen diffusion on the particle surface of $55 \pm 10\,\mathrm{kJ\,mol^{-1}}$.

- The model reproduces the weak temperature dependence of the angle distributions, which is related to a partial compensation of the temperature dependences of the diffusion coefficient, the reaction rate and the steady-state coverages.

- A quantitative description of the experiments requires trapping–desorption and direct scattering processes from the support to be taken into account, for both incoming reactants and desorbing products. Support backscattering is found to significantly broaden the angle distributions of desorbing products. In spite of this effect, strong angle dependences remain, which can be detected experimentally.

- Finally, the effect of the local angle distribution of CO_2 desorbing from a single particle facet on the total distribution of CO_2 is investigated. The experimental

data is consistent with a broad local distribution ($\cos^n$ with $n \approx 1$). Other systems with more peaked product distributions are expected to have even more pronounced angle dependence.